

The limit of quantum cascade detectors: A single period device

Benedikt Schwarz, , Peter Reininger, , Andreas Harrer, , Donald MacFarland, , Hermann Detz, , Aaron M. Andrews, , Werner Schrenk, and , and Gottfried Strasser

Citation: [Appl. Phys. Lett.](#) **111**, 061107 (2017); doi: 10.1063/1.4985711

View online: <http://dx.doi.org/10.1063/1.4985711>

View Table of Contents: <http://aip.scitation.org/toc/apl/111/6>

Published by the [American Institute of Physics](#)

Articles you may be interested in

[Degradation-induced low frequency noise and deep traps in GaN/InGaN near-UV LEDs](#)
Applied Physics Letters **111**, 062103 (2017); 10.1063/1.4985190

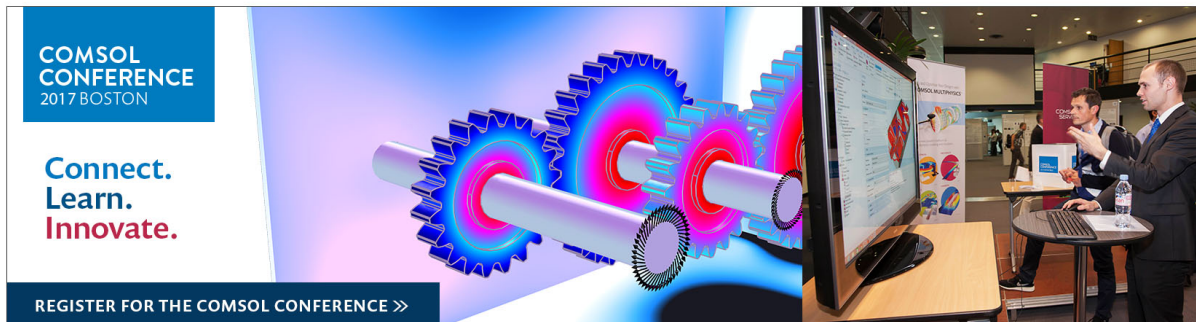
[Optically active dilute-antimonide III-nitride nanostructures for optoelectronic devices](#)
Applied Physics Letters **111**, 061101 (2017); 10.1063/1.4997450

[Phase-locked array of quantum cascade lasers with an intracavity spatial filter](#)
Applied Physics Letters **111**, 061108 (2017); 10.1063/1.4990463

[Cavity enhanced absorption spectroscopy in the mid-infrared using a supercontinuum source](#)
Applied Physics Letters **111**, 061103 (2017); 10.1063/1.4985263

[What is the best planar cavity for maximizing coherent exciton-photon coupling](#)
Applied Physics Letters **111**, 061102 (2017); 10.1063/1.4997171

[Active tuning of high-Q dielectric metasurfaces](#)
Applied Physics Letters **111**, 053102 (2017); 10.1063/1.4997301



The limit of quantum cascade detectors: A single period device

Benedikt Schwarz,^{a)} Peter Reininger, Andreas Harrer, Donald MacFarland, Hermann Detz, Aaron M. Andrews, Werner Schrenk, and Gottfried Strasser
Institute of Solid State Electronics and Center for Micro- and Nanostructures, TU Wien, Floragasse 7, 1040 Vienna, Austria

(Received 1 June 2017; accepted 15 July 2017; published online 9 August 2017)

In this work, we demonstrate a $4.1\text{ }\mu\text{m}$ quantum cascade photodetector with external quantum efficiencies of 40% at 80 K and 25% at 300 K. Such high efficiencies have been made possible by using a single period active region embedded in a facet coupled low-loss dielectric ridge waveguide. This emphasizes the relevance of enhancing the optical interaction for this type of detector in a different manner from increasing the number of periods. Low noise operation was achieved by using photovoltaic operation at zero bias and an elaborate band structure design to prevent undesired scattering paths. A noise equivalent power of $10\text{ pW}/\sqrt{\text{Hz}}$ and a corresponding specific detectivity of $7 \times 10^7\text{ cm}\sqrt{\text{Hz}}/\text{W}$ at room-temperature, as well as background limited operation below 124 K with a detectivity close to an ideal photodetector, are demonstrated. © 2017 Author(s). All article content, except where otherwise noted, is licensed under a Creative Commons Attribution (CC BY) license (<http://creativecommons.org/licenses/by/4.0/>). [<http://dx.doi.org/10.1063/1.4985711>]

Quantum cascade detectors (QCDs) are unipolar intersubband devices and are mostly designed for the detection of mid-infrared radiation.^{1–4} They can be seen as a type of photovoltaic quantum well infrared photodetector⁵ (QWIP) utilizing a ladder of subbands that act as a built-in field to extract the electrons via tunneling and longitudinal optical phonon scattering. QCDs were demonstrated using a variety of material systems.^{6–9} The choice of material does not only limit the largest possible transition energy but also have a significant impact on the performance limit of QCDs. The absorption strength, the noise performance, and the achievable performance limit for QCDs are improved with smaller effective electron mass.⁹

To push the performance of QCDs to their limit, an alternative method to achieve a high absorption efficiency, while keeping the number of periods as low as possible, has to be found. A number of strategies of enhancing the absorption efficiency of intersubband detectors have been pursued experimentally and theoretically, ranging from photonic crystal cavities,¹⁰ integrated plasmonic lenses,¹¹ to plasmonic perfect absorbers.¹² Those methods provide excellent performance and are a good choice for applications that require detection of a spatially wide beam with a narrow spectrum.

For other applications, such as detection of light from quantum cascade lasers where the spot size for detection can be very small, a dielectric ridge waveguide as absorption geometry provides several significant benefits to the device performance. They allow high absorption efficiency with a very small electric detector area, which significantly increases the device resistance and thus the signal-to-noise ratio.

Ridge waveguide based QCDs have already been used as part of the lab-on-a-chip based on bi-functional quantum cascade laser/detector materials.¹³ The idea of using ridge waveguide QCDs as external detectors has also been followed by Sakr *et al.*¹⁴ for a high speed (42 GHz 3 dB electric

bandwidth) short wavelength $\lambda = 1.55\text{ }\mu\text{m}$ detector based on the GaN/AlGaN material system and by Dougakiuchi *et al.*¹⁵ for a $\lambda = 5.4\text{ }\mu\text{m}$ detector based on InGaAs/InAlAs. At room-temperature, Dougakiuchi *et al.* achieved a responsivity of 40 mA/W in a ridge waveguide configuration with 70 periods compared to 7 mA/W for the 45° double pass mesa with 45 periods of the same QCD active region design. The minor improvement on the specific detectivity from $2.5 \times 10^7\text{ cm}\sqrt{\text{Hz}}/\text{W}$ to $3.5 \times 10^7\text{ cm}\sqrt{\text{Hz}}/\text{W}$ is due to the normalization on the optically active area. This emphasizes that ridge waveguide detectors are well suited for direct end-fire coupling, e.g., in on-chip applications and maybe for focused radiation from laser sources but not for the detection of thermal sources. In any case, ridge waveguides are a perfect geometry to demonstrate the limits of quantum cascade detectors, which is the aim of this paper.

QCDs commonly consist of 20–40 periods and thus are often designed assuming periodic boundary conditions and neglecting the interface to the bulk layers. A main reason for the large impact of the interface on the bulk regions is band bending, which can lead to a misalignment of the subbands and thus to an additional series resistance, as well as a malfunction of the first and last periods. The situation is similar to a heterojunction, with the QCD active region having an approximately 120 meV higher effective band edge than the bulk InGaAs layers. For lasers, these interfaces are commonly neglected because a small voltage drop at the interface can align the subbands and allow a sufficiently small differential resistance. However, this is not the case for zero bias operating detectors. We noted the relevance of correct interface design already in previous publications;¹⁶ however, it becomes obligatory when moving to a single period.

The band diagram of the single period active region embedded between two low doped InGaAs layers to form the waveguide core is shown in Fig. 1. The desired current path is illustrated by the black arrows. As a starting point, we used a design optimized for a grating coupled normal

^{a)}Electronic mail: benedikt.schwarz@tuwien.ac.at

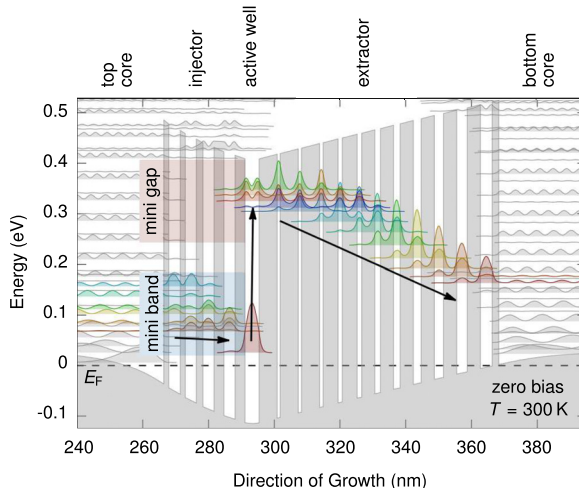


FIG. 1. Conduction band profile and subband levels of the single period active region. The consideration of the band bending induced by the interface to the bulk InGaAs layers is a key point in the design. The width of the InGaAs bulk layers in the simulation is chosen large enough to resolve the band bending.

incidence detector (20 periods)¹⁷ and modified it for single period operation. The left interface region (injector) is designed in such a way that a mini-gap is formed around the upper detector levels to prevent back scattering of excited electrons to the top InGaAs region. At the same time, a mini band allows sufficiently efficient refilling of electrons from the top waveguide core layer to the lower detector level. As we expect the prevention of back scattering to be a crucial part, we took a compromise with the mini band being located slightly to high in energy. There might be some room for improvement, but according to the experimentally obtained performance, carrier refilling does not seem to be an issue. The extractor is similar to those of conventional QCDs and provides efficient extraction of excited electrons to the bottom waveguide core layer via resonant tunneling and incoherent longitudinal optical phonon dominated scattering. Multiple coupled extractor levels have been used to ensure a certain reliability against variations between model and reality, which also results in a slightly broader spectral response. The reduction of the matrix element does not necessarily reduce the responsivity considerably, as the absorption coefficient should be sufficiently high for the ridge waveguide configuration.

The active region made from InGaAs/InAlAs, lattice matched to InP, is embedded in a waveguide similar to those used for quantum cascade lasers. A highly doped substrate and a bottom contact layer were used to prevent light coupling from the substrate. This would lead to a larger effective detector area and would make the normalization that is required for the responsivity characterization difficult. The layer structure of the entire epi-layer starting from the n^+ InP substrate is as follows, with InAlAs barriers in bold: 500 nm InGaAs ($8 \times 10^{18} \text{ cm}^{-3}$) contact layer; 1500 nm InAlAs ($1 \times 10^{17} \text{ cm}^{-3}$) waveguide cladding; 900 nm ($4 \times 10^{16} \text{ cm}^{-3}$) waveguide core; single period active region: **2**, 3.6, **4**, 3.2, **4**, 2.8, **4**, 2.4, **4**, 2.05, **4**, 1.7, **4**, 1.45, **4.5**, 1.3, **4.5**, 1.1, **5.5**, 1, **5.5**, 0.95, **5.5**, 4.3 ($8 \times 10^{17} \text{ cm}^{-3}$), **3**, 3.3, **3**, 3.3, **2**, 3.4, **1.5**, 3.5, and **1.5** ($1 \times 10^{17} \text{ cm}^{-3}$); followed by the reversed layer

structure: waveguide core, waveguide cladding, and contact layer. Chirped superlattice regions were used at all the interfaces between bulk InGaAs/InAlAs and InGaAs/InP to minimize the series resistance. The devices have been processed as 10 μm wide and 0.5 mm long ridges using UV lithography, dry etching, SiN passivation, Ti/Au sputtering, and cleaving. We did not apply an anti-reflection coating. The length of the ridges was chosen because of practical reasons and was not matched to the absorption length. Shorter ridges are expected to give a slightly better noise figure.

The spectral characterization was performed using a vacuum Fourier transform infrared spectrometer and a thermal source. In order to obtain absolute values for the responsivity, we use a calibrated thermal detector as a reference. We measured the beam spot with a motorized stage using the single period QCD. We used the entire waveguide thickness, including core and cladding, times the ridge width as the optically active “cross-sectional” area for the normalization ($5 \mu\text{m} \times 10 \mu\text{m}$), although the actual active optical area might be smaller. On the other hand, coupling through the substrate at larger incident angles can also lead to larger optical areas. We used a highly doped substrate and contact layers to minimize this coupling path and investigated the angle dependence of the coupling efficiency to check if we can indeed neglect coupling through the substrate. From this, we found that the coupling through the substrate remains smaller than 5% compared to the part that couples through the facet. The normalization on the entire waveguide thickness is conservative enough to account for this contribution. The spectra of the thermopile detector and the QCD have been measured in step-scan because of the slow response of the thermopile detector and the fact that we kept as many parameters as possible unchanged. Nevertheless, the absolute value will remain within a certain accuracy limit due to the required normalization onto the facet area. The spectral responsivity is plotted in Fig. 2 for temperatures between 80 and 300 K. We measured the responsivity to be 0.86 and 1.3 A/W, which corresponds to external quantum efficiencies of 25% and 40% at room-temperature and 80 K, respectively.

In order to investigate how close the detector is to the theoretic limit, we split the external quantum efficiency into

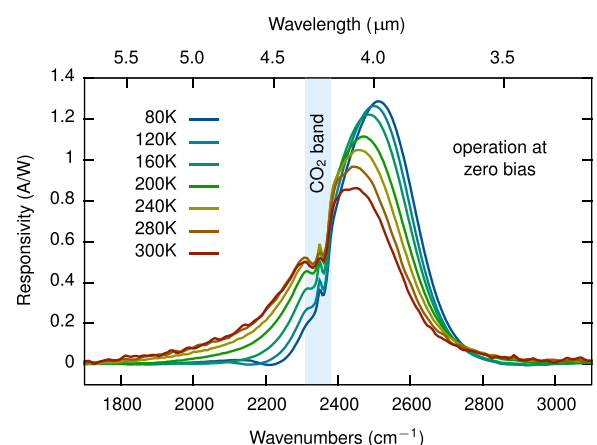


FIG. 2. Spectral responsivity of the single period ridge detector for linear polarized light. The peak responsivity and the integral of the spectral response drop by only 35% and 17% from 80 K to 300 K, respectively.

the contributions from the facet reflectivity, the probability that a photon inside the waveguide is absorbed by the active transition and the probability that an excited electron contributes to the photocurrent. The first contribution can be easily increased by 25% by applying a single layer anti-reflection coating. A better insight into the remaining two contributions can be obtained using expected efficiencies from our modeling tools. From band structure calculations and transport simulations, we expect an internal quantum efficiency >90%. From the absorption model for the ridge waveguide $\eta_{\text{abs}} = T_{\text{facet}} \Gamma \alpha_{\text{QCD}} / (\Gamma \alpha_{\text{QCD}} + \alpha_{\text{wg}}) (1 - \exp((\Gamma \alpha_{\text{QCD}} + \alpha_{\text{wg}})L))$ and the mode confinement factor Γ calculated with a 1D mode simulation, based on a home-built tool to optimize quantum cascade laser waveguides, we expect absorption efficiencies of >60%. We experimentally observed a lower resistance compared to our model, which is a hint that the doping of the active well is higher than designed. The absorption efficiency can be increased by a further increase in the doping, however, with the drawback of a reduced resistance. Due to the fact that the absorption efficiency saturates to one and that the conductivity increases superlinearly with doping, due to the shift of the Fermi-level, the Jonson noise limited detectivity of the device would decrease. A higher external quantum efficiency can only be obtained with the price of a smaller detectivity at elevated temperatures and one has to decide which property is more relevant.

The differential resistance at zero bias has been characterized in order to obtain the noise figure in the Jonson noise limit. The resulting Jonson noise limited specific detectivity is shown in Fig. 3 together with background limited specific detectivity and the differential resistance at zero bias. We want to note that the area normalization of the specific detectivity is not always useful for characterizing a ridge detector. In the case of direct end-fire coupling, e.g., from a waveguide, the signal will not scale with the optical area of the detector and the detectivity (not normalized on the area) or the noise equivalent power and a coupling coefficient are more practical parameters. The noise equivalent power at room-temperature and of the background limited infrared

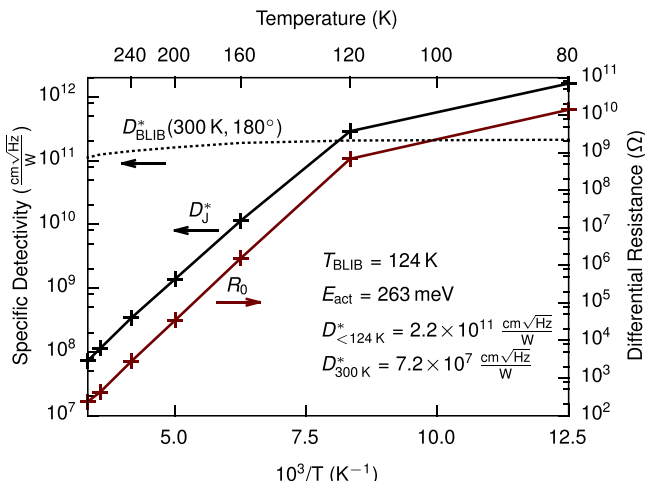


FIG. 3. Specific detectivity and differential resistance at zero bias over the inverse temperature. The differential resistance follows a straight line on the logarithmic scale that corresponds to an activation energy of $E_{\text{act}} = 263$ meV. Background limited detection has been achieved below 124 K. Temperature dependent differential resistance at zero bias.

photodetector (BLIP) at $T < 124$ K are $\text{NEP} = 10 \text{ pW}/\sqrt{\text{Hz}}$ and $3.4 \text{ pW}/\sqrt{\text{Hz}}$, respectively. The corresponding specific detectivities are $D_{\text{J},300\text{K}}^* = 7.2 \times 10^7 \frac{\text{cm}\sqrt{\text{Hz}}}{\text{W}}$ and $D_{\text{BLIP}}^* = 2.1 \times 10^{11} \frac{\text{cm}\sqrt{\text{Hz}}}{\text{W}}$. The achieved background limited detectivity is very close to that of an ideal photodetector. As a comparison, an ideal photovoltaic detector with the same spectral response would have $D_{\text{BLIP}}^* = 3.1 \times 10^{11} \frac{\text{cm}\sqrt{\text{Hz}}}{\text{W}}$, an ideal bandgap photovoltaic detector with a cut-off at $4.3 \mu\text{m}$ $D_{\text{BLIP}}^* = 2.5 \times 10^{11} \frac{\text{cm}\sqrt{\text{Hz}}}{\text{W}}$, and their photoconductive counterparts have half of the given values. One has to note that amplifier noise can be a significant limiting factor for photovoltaic detectors because of the typically small responsivity. In this case, the external quantum efficiency (or responsivity) should be optimized, which makes the reduction of the number of periods even more important.

In conclusion, we demonstrated a single period quantum cascade photodetector with a responsivity of up to 1.3 A/W . We used a low-loss dielectric ridge as absorption geometry, which allowed us to obtain very high absorption efficiencies with a single period active region. Low noise operation was achieved by preventing undesired scattering paths. We achieved a noise equivalent power of $10 \text{ pW}/\sqrt{\text{Hz}}$ at room-temperature and background limited operation below 124 K with a background limited detectivity close to that of an ideal photodetector. We envision that by utilizing more advanced coupling techniques such as fabricating an antenna, an on-chip lens or tapering of the waveguide, this type of absorption geometry can be enabled for applications with a spatially broader beam. Reducing the number of periods could also be a way to push the performance of QCDs with meta-material perfect absorption geometries or high-Q photonic crystal cavities.

The authors were supported by the Austrian Science Fund (FWF) within the framework of the projects NextLite (F4909-N23) and NanoPlas (P28914-N27), as well as by the FP7 EU-project ICARUS. H.D. acknowledges funding through an APART Fellowship of the Austrian Academy of Sciences.

- ¹D. Hofstetter, M. Beck, and J. Faist, *Appl. Phys. Lett.* **81**, 2683 (2002).
- ²L. Gendron, M. Carras, A. Huynh, V. Ortiz, C. Koeniguer, and V. Berger, *Appl. Phys. Lett.* **85**, 2824 (2004).
- ³M. Graf, N. Hoyler, M. Giovannini, J. Faist, and D. Hofstetter, *Appl. Phys. Lett.* **88**, 241118 (2006).
- ⁴A. Delga, L. Doyennette, V. Berger, M. Carras, V. Trinité, and A. Nedelcu, *Infrared Phys. Technol.* **59**, 100 (2013).
- ⁵H. Schneider and H. C. Liu, *Quantum Well Infrared Photodetectors* (Springer, Berlin, 2006).
- ⁶A. Buffaz, M. Carras, L. Doyennette, A. Nedelcu, X. Marcadet, and V. Berger, *Appl. Phys. Lett.* **96**, 172101 (2010).
- ⁷A. P. Ravikumar, J. D. Jesus, M. C. Tamargo, and C. F. Gmachl, *Appl. Phys. Lett.* **107**, 141105 (2015).
- ⁸S. Sakr, E. Giraud, A. Dussaigne, M. Tchernycheva, N. Grandjean, and F. H. Julien, *Appl. Phys. Lett.* **100**, 181103 (2012).
- ⁹P. Reininger, T. Zederbauer, B. Schwarz, H. Detz, D. MacFarland, A. M. Andrews, W. Schrenk, and G. Strasser, *Appl. Phys. Lett.* **107**, 081107 (2015).
- ¹⁰P. Reininger, B. Schwarz, R. Gansch, H. Detz, D. MacFarland, T. Zederbauer, A. M. Andrews, W. Schrenk, and G. Strasser, *Opt. Express* **23**, 6283 (2015).
- ¹¹A. Harrer, B. Schwarz, R. Gansch, P. Reininger, H. Detz, T. Zederbauer, A. M. Andrews, W. Schrenk, and G. Strasser, *Appl. Phys. Lett.* **105**, 171112 (2014).
- ¹²F. Zhao, C. Zhang, H. Chang, and X. Hu, *Plasmonics* **9**, 1397 (2014).

- ¹³B. Schwarz, P. Reininger, D. Ristanić, H. Detz, A. M. Andrews, W. Schrenk, and G. Strasser, *Nat. Commun.* **5**, 4085 (2014).
- ¹⁴S. Sakr, P. Crozat, D. Gacemi, Y. Kotsar, A. Pesach, P. Quach, N. Isac, M. Tchernycheva, L. Vivien, G. Bahir, E. Monroy, and F. H. Julien, *Appl. Phys. Lett.* **102**, 011135 (2013).
- ¹⁵T. Dougakiuchi, K. Fujita, T. Hirohata, A. Ito, M. Hitaka, and T. Edamura, *Appl. Phys. Lett.* **109**, 261107 (2016).

- ¹⁶B. Schwarz, D. Ristanic, P. Reininger, T. Zederbauer, D. MacFarland, H. Detz, A. M. Andrews, W. Schrenk, and G. Strasser, *Appl. Phys. Lett.* **107**, 071104 (2015).
- ¹⁷A. Harrer, B. Schwarz, S. Schuler, P. Reininger, A. Wirthmüller, H. Detz, D. MacFarland, T. Zederbauer, A. M. Andrews, M. Rothermund, H. Oppermann, W. Schrenk, and G. Strasser, *Opt. Express* **24**, 17041 (2016).